JMEPEG (2012) 21:1182–1187
DOI: 10.1007/s11665-011-0060-8

1059-9495/$19.00

Effect of Water Cooling on the Performances of Friction Stir Welding Heat-Affected Zone

H.J. Zhang, H.J. Liu, and L. Yu

(Submitted December 28, 2010; in revised form May 26, 2011)

The heat-affected zone (HAZ) is generally the intrinsic weakest location of the normal friction stir welded precipitate hardened aluminum alloys. In order to improve the mechanical properties of the HAZ by controlling the temperature level, underwater friction stir welding (FSW) of an Al-Cu aluminum alloy was conducted in the present study. The results indicate that the hardness of the HAZ can be improved through underwater FSW. Microstructural analysis reveals that the hardness improvement is attributed to the lowering of precipitate coarsening level and the narrowing of precipitate free zone, which are essentially induced by the variations of welding thermal cycles under the cooling effect of water.

Keywords aluminum, mechanical testing, welding

1. Introduction

Friction stir welding (FSW), as a solid state joining process, has been successfully utilized to weld various precipitate hardened aluminum alloys (Ref 1-3). However, it has been demonstrated that FSW tends to create a softening region in the joints due to the dissolution or growth of the strengthening precipitates during the welding, thus leading to a degradation of mechanical properties of the joints (Ref 4-7). The softening region consists of the weld nugget zone (WNZ), the thermal mechanically affected zone (TMAZ), and the heat-affected zone (HAZ). Generally, the HAZ is the weakest location of the joints since it experiences the greatest coarsening and transformation of meta-stable precipitates but does not achieve the sufficient temperature for reprecipitation (Ref 8-11). Accordingly, improving the mechanical properties of the HAZ is crucial to the optimization of the whole joint performances. In order to weaken the negative effect of thermal cycles on the HAZ and improve the mechanical properties of the joints, external liquid cooling has been applied during FSW in several investigations. Benavides et al. (Ref 12) developed FSW experiment of 2024 aluminum alloy using liquid nitrogen cooling to decrease the initial temperature of plates to be welded from 30 to −30 °C. It was found that the hardness of the HAZ was remarkably improved, but void defect was formed in the WNZ and the hardness-microstructure relationship was not clarified.

Fratini et al. (Ref 13) and the present authors (Ref 14) considered water as the cooling liquid to exert an in-process heat treatment on welding samples during FSW. Likewise, a notable hardness improvement was observed in the HAZ. However, the microstructural evolution dominantly causing the hardness improvement was still not illuminated. In this article, a 2219-T6 aluminum alloy was friction stir welded under two kinds of circumstances. One is in air, and the other is under water. The purpose of the present study is to clarify the intrinsic reason for the hardness improvement in the HAZ from the aspects of microstructures and welding thermal cycles when external liquid cooling is applied during FSW.

H.J. Zhang, H.J. Liu, and **L. Yu**, State Key Laboratory of Advanced Welding Production Technology, Harbin Institute of Technology, Harbin 150001, People's Republic of China. Contact e-mails: xfwineer@yahoo.cn and liuhj@hit.edu.cn.

2. Experimental Procedure

The base metal (BM) was a 7.5-mm-thick 2219-T6 aluminum alloy plate, whose chemical compositions and mechanical properties are listed in Table 1. The plate was cut and machined into rectangular welding samples of 300 mm long by 100 mm wide. FSW experiments were carried out under two kinds of circumstances. One is in air, and the other is under water. For the convenience of statement, the FSW performed in air is defined as normal FSW, and the HAZ of the normal joint is called NHAZ; while the FSW performed under water is defined as underwater FSW, and the HAZ of the underwater joint is called UHAZ. Figure 1(a) shows the schematic view of underwater FSW process. Butt welds were made along the longitudinal direction (perpendicular to the rolling direction) of the samples using an FSW machine. The maximum rotation speed, welding speed, and axial load for the machine are 3000 rpm, 1200 mm/min, and 20 kN, respectively. The welding tool and the parameters used for normal and underwater FSW were the same. The welding tool consisted of a 22.5-mm diameter shoulder and a conical right-hand screwed pin with the length of 7.4 mm and the median diameter of 7.4 mm. The rotation speed, welding speed, and axial load were 800 rpm, 100 mm/min, and 4.6 kN, respectively.

After welding, all the joints were cross-sectioned perpendicular to the welding direction for metallographic analyses and Vicker's hardness test using an electrical-discharge cutting machine. The cross sections of the metallographic specimens were polished with a diamond paste, etched with Keller's

Table 1 Chemical compositions and mechanical properties of 2219-T6 aluminum alloy

Chemical compositions, wt.%									Mechanical properties	
Al	Cu	Mn	Fe	Ti	V	Zn	Si	Zr	Tensile strength	Microhardness
Bal.	6.48	0.32	0.23	0.06	0.08	0.04	0.49	0.20	432 MPa	120-130 Hv

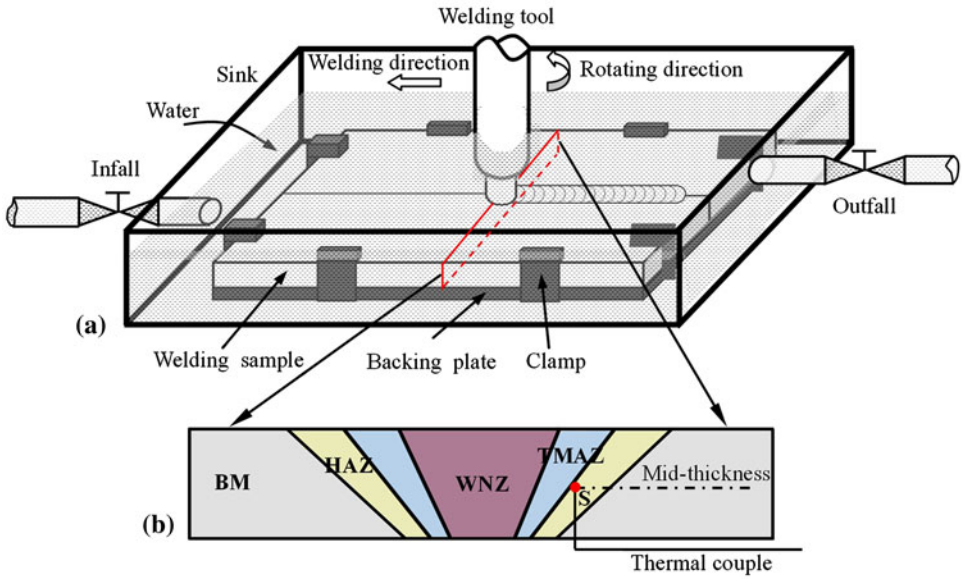

Fig. 1 Schematic of (a) underwater FSW, (b) cross section of the joint. Note that the Point S adjacent to the TMAZ/HAZ boundary was determined by microstructural differences between HAZ and TMAZ

reagent, and observed by optical microscopy (OM). Vicker's hardness testing was carried out at the mid-thickness of the polished cross sections with a spacing of 1 mm. The testing load was 4.9 N for 10 s.

The foil disk specimens for transmission electron microscopy (TEM) were cut parallel to the welding direction from the HAZ adjacent to the TMAZ (i.e., Point S marked in Fig. 1b) and the BM at weld mid-thickness. The specimens were first machined and manually polished down to a thickness of 100 μm. The final thickness reduction was acquired by electropolishing with a HNO_3 solution (HNO_3 30% in volume in methanol at −35 °C under 18 V).

The transverse tensile specimens were cut perpendicular to the welding direction. The room temperature tensile test was carried out at a crosshead speed of 1 mm/min using a computer-controlled testing machine, and the tensile properties of each joint were evaluated using three tensile specimens cut from the same joint. After tensile test, the OM above mentioned was utilized to analyze the fracture features of the joints.

K-type thermocouples were used to measure the temperature of the samples during FSW. The tips of thermocouples were located at Point S to evaluate the welding thermal cycles of the HAZ (see Fig. 1b).

3. Results and Discussion

3.1 Hardness Distributions in the HAZ

The cross sections of the HAZ are shown in Fig. 2(a) and (b), and the corresponding hardness profiles in the scanning paths denoted by the arrows in Fig. 2(a) and (b) are given in Fig. 2(c). The hardness profiles were started from Point S and extended to the BM. Since the HAZ presents lower hardness value than the BM, the HAZ width can be evaluated from the hardness profiles. Evidently, the width of UHAZ is much smaller than that of NHAZ. In addition, it is interesting to find that the hardness of UHAZ is remarkably higher than that of NHAZ. The minimum hardness value of UHAZ is 92 Hv, while that of NHAZ is only 78 Hv, indicating an improvement in mechanical properties of the HAZ via underwater FSW.

The hardness improvement in the HAZ is benefit to the tensile properties of the whole joint. The normal joint, with tensile strength of 324 MPa, is fractured in the HAZ adjacent to the TMAZ during tensile test (see Table 2), indicating that the HAZ is the intrinsic weakest location of the joint. When external water cooling is applied, a tensile strength of 341 MPa is obtained, higher than that of the normal joint. The underwater joint is fractured nearly along the WNZ/TMAZ interface rather than in the HAZ due to the hardness improvement in the HAZ.

The variation of hardness distributions must be coupled with the microstructural evolution; hence, it is necessary to investigate the microstructural characteristics in the HAZ to illuminate the hardness profiles presented in Fig. 2(c).

3.2 Microstructural Evolution Induced by Water Cooling Action

Figure 3 shows the grain structures of the BM and the HAZ. The grains of NHAZ and UHAZ exhibit the similar size and shape to the BM, indicating that little variations of grained structures have occurred in the HAZ during both normal and

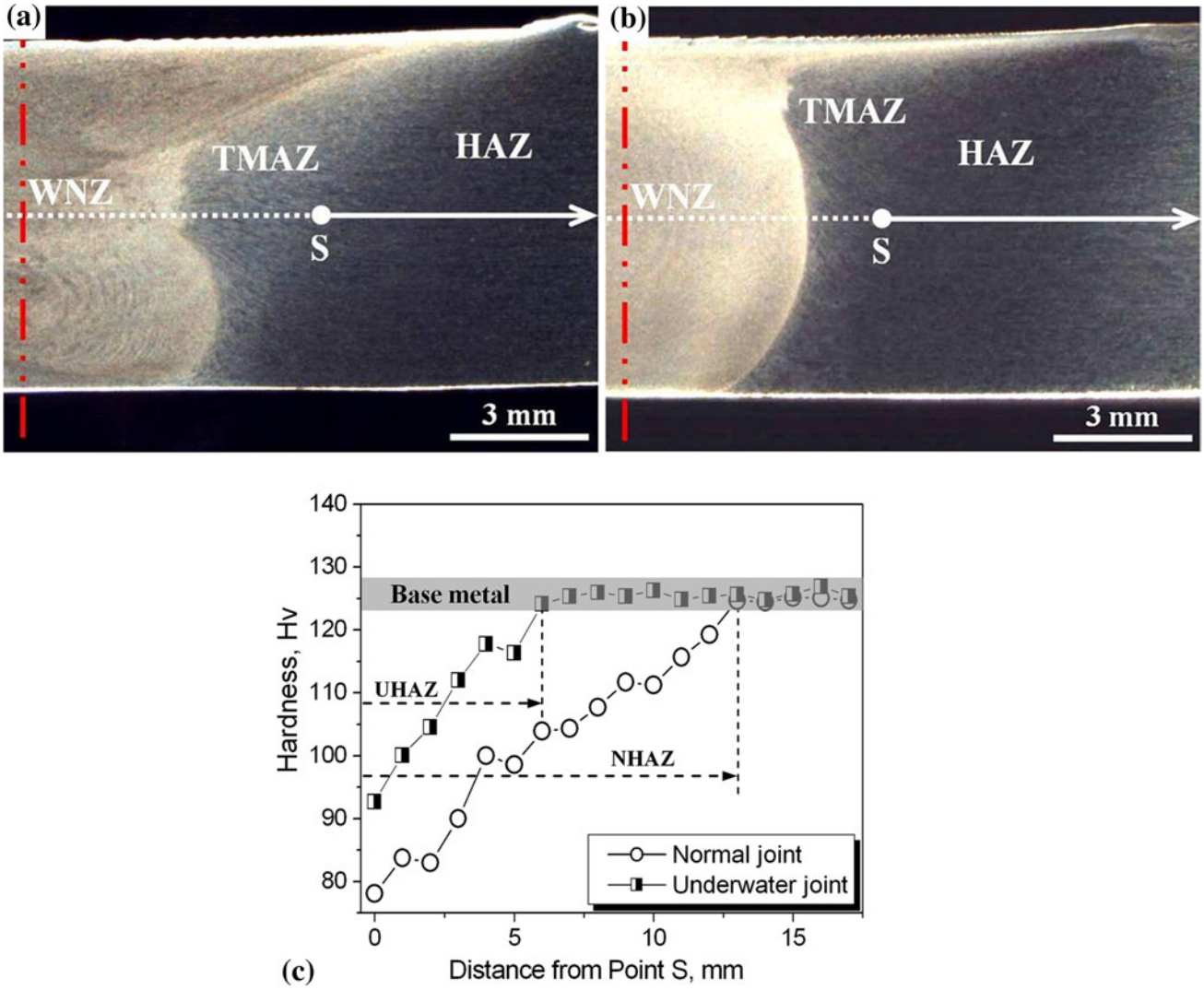

Fig. 2 Cross sections and hardness profiles of the HAZ: (a) cross section of the NHAZ, (b) cross section of the UHAZ, (c) hardness profiles of the HAZ. In "a" and "b", the horizontal dashed line is denoted as weld midplane, and the vertical line represents weld centerline

Table 2 Tensile behavior of the joints

Welding condition	Sample	Tensile strength, MPa	Average, MPa	Fracture locations	
				Top surface	Typical cross section
Normal	1	323	324	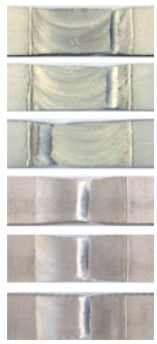	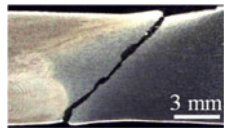
	2	326			
	3	323			
Underwater	1	340	341		
	2	342			
	3	341			

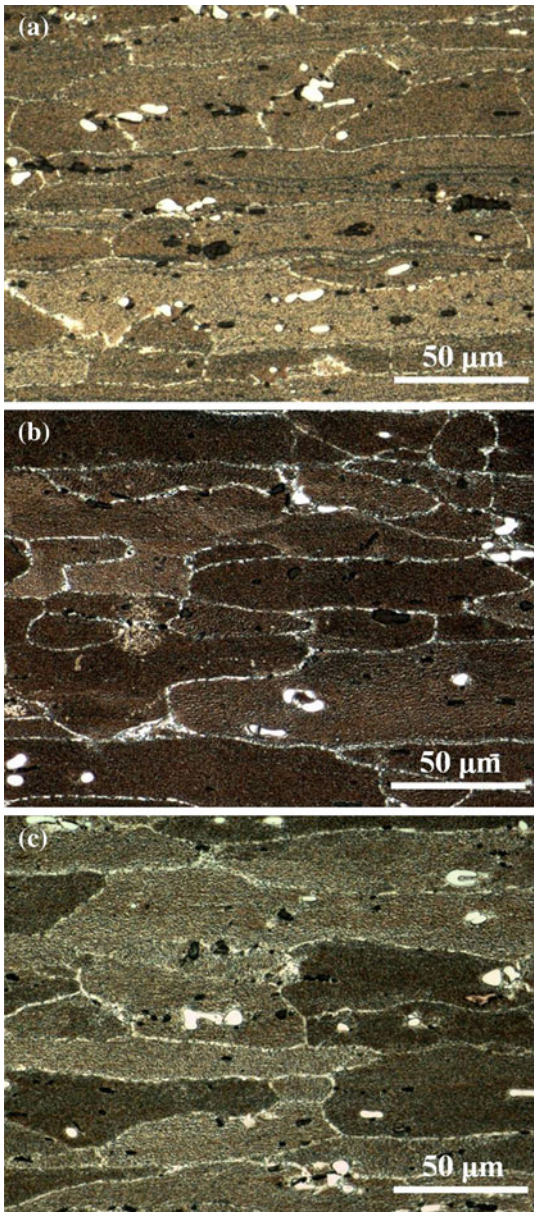

Fig. 3 Grain structures of the BM and the HAZ: (a) BM, (b) NHAZ, and (c) UHAZ

underwater FSW. Therefore, the grain size is not the main reason for hardness difference between NHAZ and UHAZ.

The white precipitates in the BM (see Fig. 3a), formed during the aging process of the alloy, are identified as the Al_2Cu intermetallics from the energy dispersive spectrometer (EDS) analysis. In contrast to the BM, the relative thick grain boundaries (GBs) in Fig. 3(b) and (c) indicate that precipitate coarsening has occurred in the HAZ during FSW. To reveal the precipitate morphologies more clearly, Fig. 4 shows the TEM micrographs of the precipitates in the BM and the HAZ, which are extracted from the {100} planes of the matrix. The plate-shaped precipitates in the BM and the HAZ are found to be θ′ phases according to the electron diffraction patterns. The size of the precipitates distributed in the BM is 54 ± 24 nm in diameter and 4 ± 1.8 nm in thickness. In the NHAZ, the θ′ precipitates experience a significant coarsening and density decrease. The precipitates in the NHAZ have a diameter of 106 ± 28 nm and

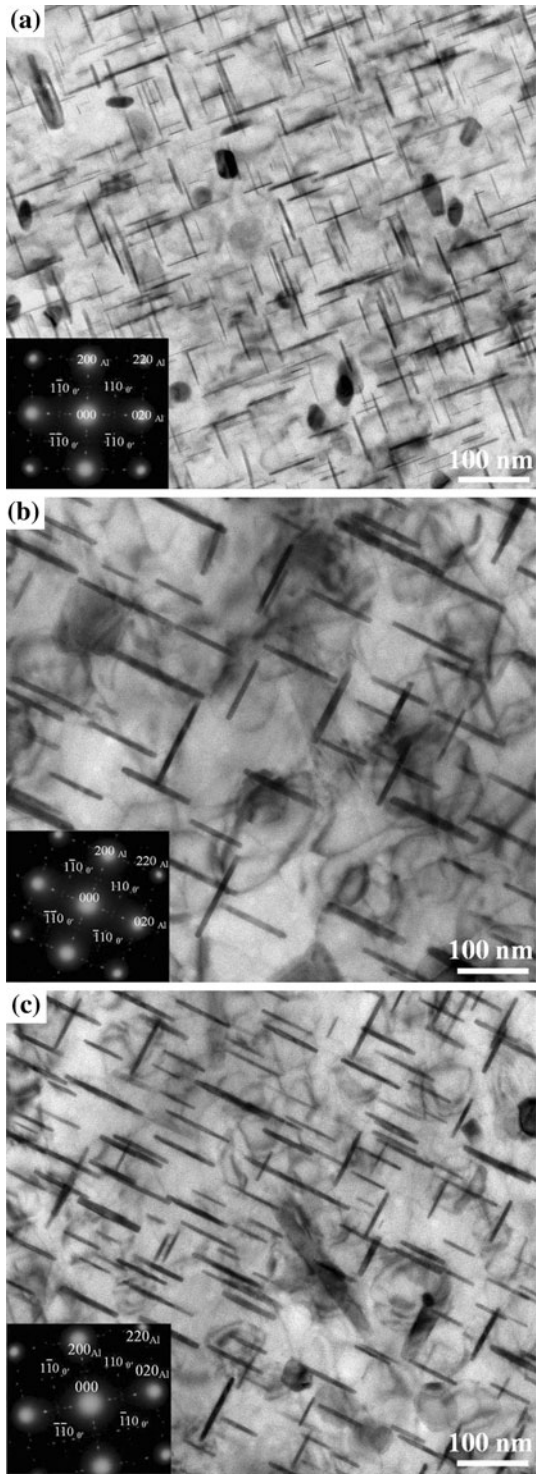

Fig. 4 The precipitates of the BM and the HAZ: (a) BM, (b) NHAZ, and (c) UHAZ

a thickness of 10 ± 2.6 nm, much larger than the size observed in the BM. In the UHAZ, the extent of precipitate coarsening is lowered because the diameter and the thickness of the precipitates only reach 92 ± 30 and 7 ± 1.8 nm, respectively. The precipitate coarsening level depends on the diffusion of solute atoms from aluminum matrix to precipitates. It appears that the net diffusional contribution to precipitate coarsening becomes lower in the HAZ when external water cooling is

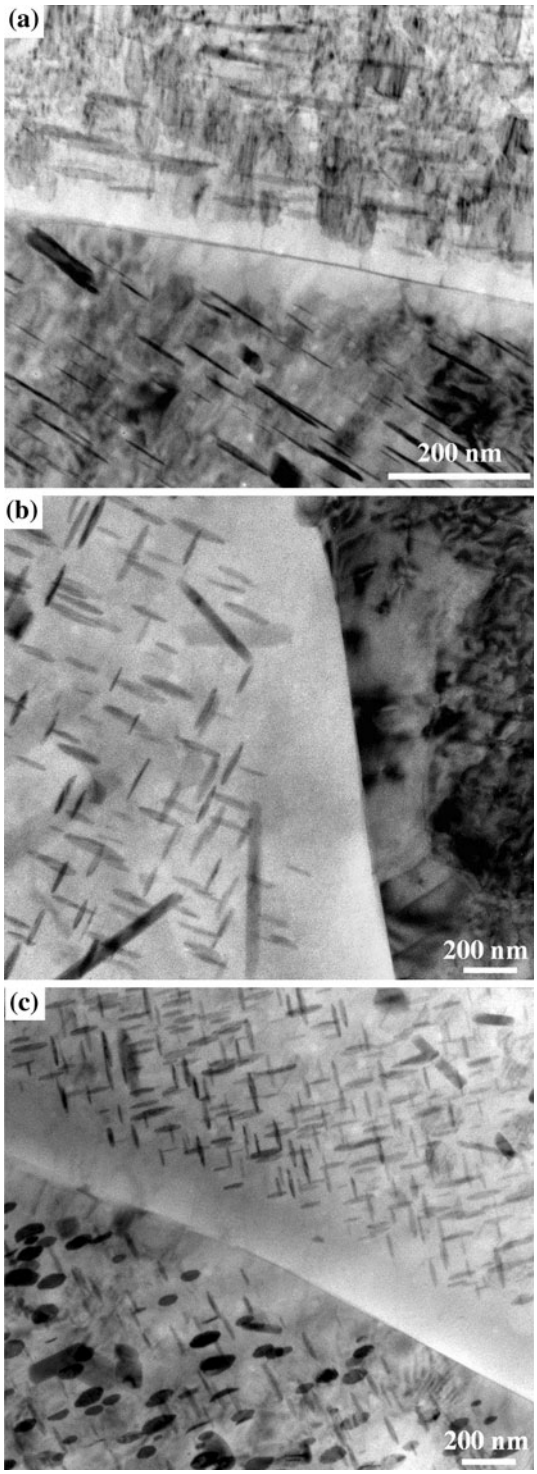

Fig. 5 The precipitate free zones of the BM and the HAZ: (a) BM, (b) NHAZ, and (c) UHAZ

employed during FSW, which restricts the coarsening of θ′ precipitates and thus enhances the precipitate hardening effect.

On the other hand, precipitate free zones (PFZs) are observed in the BM and the HAZ, as seen from Fig. 5. With regard to precipitate hardened aluminum alloys, it is known that PFZ tends to be formed along the GBs during the aging process of the alloys (Ref 15, 16). In the present study, the width of PFZ, defined as the average distance between the GB and the region

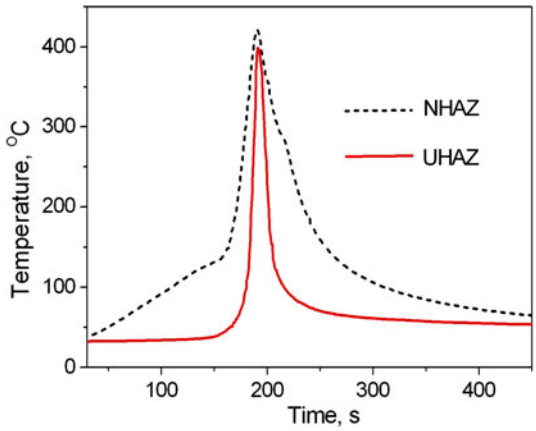

Fig. 6 Time-temperature history profiles of Point S

with extensive precipitates, is an average value of three PFZs from the same region. A small PFZ is evident along the GB in the BM, about 100 ± 12 nm in width (Fig. 5a). In the NHAZ, the width of PFZ has increased to 400 ± 25 nm (Fig. 5b), much larger than that of the BM. Interestingly, the PFZ in the UHAZ only has a width of 280 ± 16 nm (Fig. 5c). The precipitates are coarsened in the HAZ in contrast to the BM during FSW, as above described. The precipitate coarsening near the GBs depletes a large amount of solute atoms, which is responsible for the widening of PFZ. Compared with the NHAZ, the relatively narrow PFZ of the UHAZ should be attributed to the lower level of precipitate coarsening. Many investigations have revealed that the formation and growth of PFZ along the GBs exert negative effects on mechanical properties of the materials (Ref 17-19). The decrease in PFZ width is thereby also responsible for the hardness improvement in the UHAZ.

3.3 Welding Thermal Cycles of the HAZ

The precipitate evolution in the HAZ is essentially determined by the welding thermal cycles during FSW. Figure 6 shows the time-temperature history profiles of Point S in both NHAZ and UHAZ. The thermocouple records a peak temperature of 420 °C in the NHAZ, while a peak temperature of 398 °C is obtained in the UHAZ, lower than that of the NHAZ. As the tool passes by the measured point, the temperature of NHAZ gradually increases to the peak value and then shows a slow cooling rate. While for UHAZ, the temperature does not increase until the tool reaches the measured point. After the tool moves away, the water produces strong cooling effect on the workpiece, leading to a sudden decrease in temperature. This makes the UHAZ experience shorter time at higher temperature than the NHAZ. Since the water cooling action effectively lowers the peak temperature and shortens the high temperature dwelling time, the precipitate coarsening can be restricted and the widening of PFZ is also controlled, which finally results in the hardness improvement in the HAZ.

4. Conclusions

(1) The hardness of the UHAZ is improved in contrast to the NAHZ, resulting in the variation of tensile behavior and the improvement in mechanical properties of the underwater joint.

(2) The lowering of precipitate coarsening level and the narrowing of PFZ are responsible for the hardness improvement in the UHAZ.
(3) The controlling of welding thermal cycles by the water cooling effect is the intrinsic reason for variations of microstructures and mechanical properties in the HAZ during underwater FSW.

Acknowledgments

The authors are grateful to be supported by the National Basic Research Program of China (973 Program, 2010CB731704) and by the National Science and Technology Major Project of China (302010ZX04007-011).

References

1. M.R. Johnsen, Friction Stir Welding Takes Off at Boeing, *Weld. J.*, 1999, **78**, p 35–39
2. D. Joelj, The Friction Stir Welding Advantage, *Weld. J.*, 2001, **80**, p 30–34
3. R.S. Mishra and Z.Y. Ma, Friction Stir Welding and Processing, *Mater. Sci. Eng. Rep.*, 2005, **50**, p 1–78
4. G. Liu, L.E. Murr, C.S. Niou, J.C. Mcclure, and F.R. Vega, Microstructural Aspects of the Friction-Stir Welding of 6061-T6 Aluminum, *Scripta Mater.*, 1997, **37**, p 355–361
5. H.J. Liu, H. Fujii, M. Maeda, and K. Nogi, Tensile Properties and Fracture Locations of Friction-Stir Welded Joints of 6061-T6 Aluminum Alloy, *J. Mater. Sci. Lett.*, 2003, **22**, p 1061–1063
6. W.A. Baeslack, K.V. Jata, and T.J. Lienert, Structure, Properties and Fracture of Friction Stir Welds in a High-Temperature Al-8.5Fe-1.3V-1.7Si Alloy (AA-8009), *J. Mater. Sci.*, 2006, **41**, p 2939–2951
7. M. Cabibbo, H.J. McQueen, E. Evangelista, S. Spigarelli, M. Di Paola, and A. Falchero, Microstructure and Mechanical Property Studies of AA6056 Friction Stir Welded Plate, *Mater. Sci. Eng. A*, 2007, **460- 461**, p 86–94
8. R.W. Fonda and J.F. Bingert, Microstructural Evolution in the Heat-Affected Zone of a Friction Stir Weld, *Metall. Mater. Trans. A*, 2004, **35**, p 1487–1499
9. T.S. Srivatsan, S. Vasudevan, and L. Park, The Tensile Deformation and Fracture Behavior of Friction Stir Welded Aluminum Alloy 2024, *Mater. Sci. Eng. A*, 2007, **466**, p 235–245
10. A. Sullivan and J.D. Robson, Microstructural Properties of Friction Stir Welded and Post-Weld Heat-Treated 7449 Aluminium Alloy Thick Plate, *Mater. Sci. Eng. A*, 2008, **478**, p 351–360
11. M.J. Starink, A. Deschamps, and S.C. Wang, The Strength of Friction Stir Welded and Friction Stir Processed Aluminium Alloys, *Scripta Mater.*, 2008, **58**, p 377–382
12. S. Benavides, Y. Li, L.E. Murr, D. Brown, and J.C. McClure, Low-Temperature Friction-Stir Welding of 2024 Aluminum, *Scripta Mater.*, 1999, **41**, p 809–815
13. L. Fratini, G. Buffa, and R. Shivpuri, In-Process Heat Treatments to Improve FS-Welded Butt Joints, *Int. J. Adv. Manuf. Technol.*, 2009, **43**, p 664–670
14. H.J. Liu, H.J. Zhang, and L. Yu, Homogeneity of Mechanical Properties of Underwater Friction Stir Welded 2219-T6 Aluminum Alloy, *JMEPEG*, doi:10.1007/s11665-010-9787-x
15. A. Tolley, D. Mitlin, V. Radmilovic, and U. Dahmen, Transmission Electron Microscopy Analysis of Grain Boundary Precipitate-Free-Zones (PFZs) in an AlCuSiGe Alloy, *Mater. Sci. Eng. A*, 2005, **412**, p 204–213
16. B. Cai, B.L. Adams, and T.W. Nelson, Relation Between Precipitate-Free Zone Width and Grain Boundary Type in 7075-T7 Al Alloy, *Acta Mater.*, 2007, **55**, p 1543–1553
17. G. Ran, J.E. Zhou, and Q.G. Wang, Precipitates and Tensile Fracture Mechanism in a Sand Cast A356 Aluminum Alloy, *J. Mater. Process. Technol.*, 2008, **207**, p 46–52
18. G. Itoh, M. Kanno, T. Hagiwara, and T. Sakamoto, Embrittlement in an Age-Hardened 2091 Aluminum Alloy by Exposure at Elevated Temperatures Below the Aging Temperature, *Acta Mater.*, 1999, **47**, p 3799–3809
19. M.J. Starink, P. Wang, I. Sinclair, and P.J. Gregson, Microstructure and Strengthening of Al-Li-Cu-Mg Alloys and MMCs: II. Modelling of Yield Strength, *Acta Mater.*, 1999, **47**, p 3855–3868